Supporting Information

Cooperative catalysis between Ce^{3+} sites and Ag nanoparticles enabling nonoxidative coupling of methane to ethane

Song-Ye Zeng,[a] Min Wang,[a] Yin-Feng Wang,[a] Chang-Long Tan,*[b] Ming-Yu Qi,*[b] Yi-Jun Xu,[a,b] and Zi-Rong Tang*[a,b]

[a] College of Chemistry, State Key Laboratory of Photocatalysis on Energy and Environment, Fuzhou University, Fuzhou 350116, P. R. China

[b] School of Materials and Energy & Institute of Fundamental and Frontier Sciences, University of Electronic Science and Technology of China, Chengdu 611731, P. R. China.

E-mail: cl_tan@uestc.edu.cn; myqi@uestc.edu.cn; zrtang@uestc.edu.cn

Table of Contents

Experimental section

Fig. S1. TEM image of $Ag_{0.7}/CeO_2$.

Fig. S2. (a) Tauc plot for optical-band-gap determination of CeO_2. (b) Mott-Schottky plot for CeO_2 in a 0.2 M Na_2SO_4 aqueous solution (pH = 7).

Fig. S3. (a) Tauc plot for optical-band-gap determination of $Ag_{0.7}/CeO_2$. (b) Mott-Schottky plot for $Ag_{0.7}/CeO_2$ in a 0.2 M Na_2SO_4 aqueous solution (pH = 7).

Fig. S4. High-resolution XPS spectra of CeO_2 and $Ag_{0.7}/CeO_2$.

Fig. S5. EPR spectra of CeO_2 and $Ag_{0.7}/CeO_2$.

Fig. S6. GC data for photocatalytic CH_4 conversion over (a) CeO_2 and (b) $Ag_{0.7}/CeO_2$.

Fig. S7. The production rate of carbonaceous products in photocatalytic NOCM after 2 h light irradiation.

Fig. S8. EPR spectra of $Ag_{0.7}/CeO_2$-T (T = 500, 800, 1000, 1100).

Fig. S9. Catalyst temperature variation during (a) AQY measurements and (b) regular reaction process.

Fig. S10. (a) Mass spectra of C_2H_6 produced over $Ag_{0.7}/CeO_2$ using $^{12}CH_4$ (1 atm) as the reactant. (b) Mass spectra of C_2H_6 produced over $Ag_{0.7}/CeO_2$ using $^{13}CH_4$ (1 atm) as the reactant.

Fig. S11. Comparative experiments of $Ag_{0.7}/CeO_2$ catalyst under different conditions.

Fig. S12. Time-dependent photocatalytic C_{2+} production over $Ag_{0.7}/CeO_2$.

Fig. S13. In situ Ag 3*d* XPS spectra of $Ag_{0.7}/CeO_2$ under the dark condition and light irradiation.

Fig. S14. In situ FT-IR spectra of photocatalytic conversion of CH_4 over CeO_2.

Fig. S15. Illustration of photoredox catalytic mechanism for nonoxidative coupling of CH_4 over $Ag_{0.7}/CeO_2$.

Table S1. ICP results for all composite samples.

Table S2. The ratios of Ce^{3+} and lattice oxygen (O_{latt}) on different samples.

Table S3. Distribution of Brønsted and Lewis acids for CeO_2 and $Ag_{0.7}/CeO_2$.

Table S4. Representative works on photocatalytic nonoxidative coupling of CH_4 to C_2H_6 under identical conditions.

Table S5. Kinetic analysis of emission decay for CeO_2 and $Ag_{0.7}/CeO_2$.

References

Experimental section

1. Chemicals and Materials. Ethylene glycol, ethanol, polyvinyl pyrrolidone (PVP, K30), silver nitrate ($AgNO_3$), and cerium nitrate ($Ce(NO_3)_3·6H_2O$) were purchased from the Sinopharm Chemical Reagent Co., Ltd. All materials were of analytical grade and used without further purification.

2. Synthesis of CeO_2 nanospheres. In a typical synthesis, 5 g of $Ce(NO_3)_3·6H_2O$ and 2 g of polyvinyl pyrrolidone were dissolved in a mixed solution of ethylene glycol and deionized water (volume ratio 1:15). After continuous stirring for 1 h, the solution was transferred into a 100 mL Polytetrafluoroethylene-lined reaction kettle. The mixture was heated to 160 ℃ and kept at this temperature for 8 h. After naturally cooled to room temperature, it was centrifuged with deionized water for several times, and then dried in an oven at 80 ℃ for 12 h to obtain cerium acetate. Finally, the cerium acetate was calcined at 800 ℃ in air for 3 h to obtain CeO_2 nanosphere powder.

3. Synthesis of Ag_x/CeO_2 composites. The Ag_x/CeO_2 composites were prepared by the photodeposition method. Specifically, 20 mg of the prepared CeO_2 powder was dispersed in a mixture of water and ethanol (volume ratio 4:1) and injected with a certain amount of 1 mg/mL $AgNO_3$ aqueous solution, and then fully sonicated for 10 min. The suspension was irradiated with a 300 W xenon lamp under a nitrogen atmosphere for 30 min. The resulting samples were washed with deionized water and dried at 60 ℃ overnight. The loading ratio of Ag was changed by adjusting the amount of $AgNO_3$ aqueous solution. The resulting sample was denoted as Ag_x/CeO_2, where x represents the mass percentage of Ag (x = 0.0, 0.3, 0.5, 0.7, 0.9, 1.1).

4. Synthesis of CeO_2-T nanospheres. The cerium acetate was calcined at T ℃ in air for 3 h to obtain CeO_2-T nanosphere powder, where T represents the annealing temperature of CeO_2 (T = 500, 800, 1000, 1100).

5. Synthesis of $Ag_{0.7}/CeO_2$-T composites. The $Ag_{0.7}/CeO_2$-T composites were prepared by the photodeposition method. Specifically, 20 mg of the prepared CeO_2-T powder was dispersed in a mixture of water and ethanol (volume ratio 4:1) and injected with a certain amount of 1 mg/mL $AgNO_3$ aqueous solution, and then fully sonicated for 10 min. The suspension was irradiated with a 300 W xenon lamp under a nitrogen atmosphere for 30 min. The resulting samples were washed with deionized water and dried at 60 ℃ overnight. The resulting sample was denoted as $Ag_{0.7}/CeO_2$-T.

6. Photoactivity testing. Photocatalytic methane (CH_4) conversion was performed at atmospheric pressure and room temperature to evaluate the photocatalytic CH_4 conversion performance of the prepared samples. FTO glass dispersed with 1 mg photocatalyst was placed in a sealed quartz reactor. Subsequently, the reactor was purged with argon for 15 min to remove air from the system completely. Before illumination, 1 mL (44.6 μmol) of CH_4 was introduced into the reactor and left in the dark for 1 h to achieve CH_4 gas adsorption/desorption equilibrium. Afterward, the reactor was irradiated by an Xe lamp with a UV-vis light source (320 nm < λ < 780 nm). The incident light intensity was 800 mW cm^{-2} as measured by a photoradiometer (PL-MW2000, Beijing Perfectlight Technology Co., Ltd.). After the reaction, a gas chromatograph (Shimadzu GC-8A 2014C) equipped with a flame ionization detector (FID) and a thermal conductivity detector (TCD) was used for the determination of carbon oxide and H_2 in the reaction gas. Gas chromatography (Agilent 7820A) was used for the analysis of CH_4 and hydrocarbons in the reaction gas. In isotope labeling experiments, the produced C_2H_6 was analyzed using gas chromatography-mass spectrometry (Shimadzu GC-MS QP 2020, Q-Exactive).

7. Experiment of cycle reaction. For the recycle tests, each cycle lasted 2 h. The samples were collected after the reaction and then activated by heating in air at 60 °C for 1h to ensure that the lattice oxygen of CeO_2 was restored before the next test.

8. Characterization. The morphology and elemental distribution of the samples were analyzed by field emission

scanning electron microscopy (FESEM) on the FEI Nova NANO-SEM 230 spectrophotometer and transmission electron microscopy (TEM), high-resolution TEM (HRTEM) and elemental mapping analysis using a JEOL 2100F instrument at an accelerating voltage of 200 kV. The X-ray diffraction (XRD) patterns of samples were measured on a Bruker D8 Advance X-ray diffractometer with Cu K_α radiation in the 2ϑ ranging from 10 to 90° at a scan rate of 0.02° s^{-1}. UV-vis diffuse reflectance spectroscopy (DRS) on UV-vis Spectrophotometers (Thermo Scientific Evolution 200 Series) was used to measure the optical properties of the samples with $BaSO_4$ as the internal reflectance standard. X-ray photoelectron spectroscopy (XPS) measurements were performed using a Thermo Fisher Scientific K-Alpha that consists of monochromatic Al *Kα* as the X-ray source, a hemispherical analyzer, and a sample stage with multiaxial adjustability to obtain the composition on the surface of the samples. All of the binding energies were calibrated using the C 1*s* peak of the surface adventitious carbon at 284.8 eV. The electron paramagnetic resonance (EPR) signal of the radical spin-trapped by 5,5- dimethyl-1-pyrroline-*N*-oxide (DMPO) was measured on a Bruker EPR A300 spectrometer. The pyridine adsorption infrared spectra were performed on a Tensor 27 Fourier transform infrared spectrometer (Bruker Optics, Germany). The photoelectrochemical and electrochemical analyses were conducted in a conventional three electrode cell with a Pt plate as the counter electrode and an Ag/AgCl electrode as the reference electrode and reference electrode, respectively. The working electrode was prepared on fluorine doped tin oxide (FTO) glass that was cleaned by sonication in ethanol and deionized water and then dried at 60 °C for 3 h. The boundary of FTO glass was protected using Scotch tape. 5 mg sample was fully dispersed in 1 mL DMF and ethanol mix solvent by sonication to get a slurry. The slurry (15 µL) was spread onto the pre-treated FTO glass. The working electrode was dried at 80 °C for 1 h to improve adhesion. Then, the scotch tape was unstuck, and the uncoated part of the electrode was isolated with epoxy resin. The exposed area of the working electrode was 0.20 cm^2. The electrochemical impedance spectroscopy (EIS) experiments were conducted on an electrochemical workstation (Autolab, PGSTAT204) in the electrolyte of 0.5 M KCl aqueous solution containing 0.01 M $K_3[Fe(CN)_6]/K_4[Fe(CN)_6]$ (1:1) under open-circuit potential conditions. The cyclic voltammograms (CV) were measured in the same solution in the three-electrode cells as that of the EIS measurements. Mott Schottky plots were recorded at three frequencies (500, 1000, and 1500 Hz) with a bias potential that ranged from –1 to 1 V *vs.* Ag/AgCl. The transient photocurrent density was measured in 0.2 M Na_2SO_4 aqueous solution (pH = 7). The cathodic polarization curves were obtained using the linear sweep voltammetry (LSV) technique with a scan rate of 0.005 mV s^{-1} in a 0.1 M Na_2SO_4 aqueous solution. The photoluminescence (PL) spectra for samples were analyzed on an Edinburgh Analytical Instrument F900 spectrophotometer with an excitation wavelength of 340 nm. To ensure the comparability of the PL spectra, the experimental parameters, including the excitation wavelength, slit width, and the amount of the samples, were identical. The elemental concentration analysis was performed using an inductively coupled plasma emission spectroscopy instrument (ICP, Agilent ICPOES730). The temperature programmed desorption of CH_4 (CH_4-TPD) experiment was performed on a BelCata II apparatus. In situ high-resolution X ray photoelectron spectra in dark and under light irradiation were acquired on a Thermo Scientific ESCALAB 250Xi X-ray photoelectron spectrometer (Thermo Fisher Scientific, USA). The Fourier transform-infrared (FT-IR) spectra were recorded on a Thermo IS-50 FTIR spectrometer. A 300 W Xe lamp (PLS-SXE 300D, Beijing Perfectlight Technology Co., Ltd.) was used as the irradiation source.

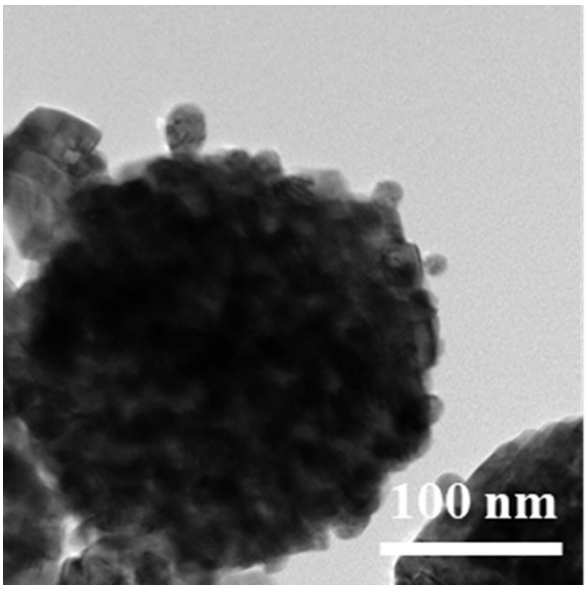

Fig. S1. TEM image of $Ag_{0.7}/CeO_2$.

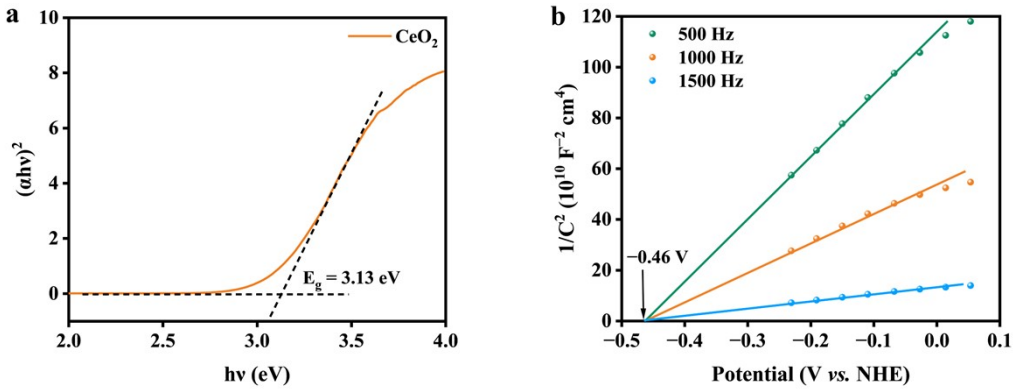

Fig. S2. (a) Tauc plot for optical-band-gap determination of CeO_2. (b) Mott-Schottky plot for CeO_2 in a 0.2 M Na_2SO_4 aqueous solution (pH = 7).

Note: To calculate the band gap energy, the following formula is used[S1]:

$$(\alpha h\nu)^2 = K \cdot (h\nu - E_g)$$

where α is the absorption coefficient, hν is the photon energy, K is a constant, and E_g is the band gap energy. As shown in **Fig. S2a**, the band gap of CeO_2 is evaluated to be 3.13 eV. In addition, the flat band position which refers to the conduction band (CB) of CeO_2 is estimated at −0.46 V *vs.* normal hydrogen electrode (NHE) according to the Mott-Schottky analysis (**Fig. S2b**). The valence band (VB) of CeO_2 is then calculated with the value of 2.67 V *vs.* NHE.

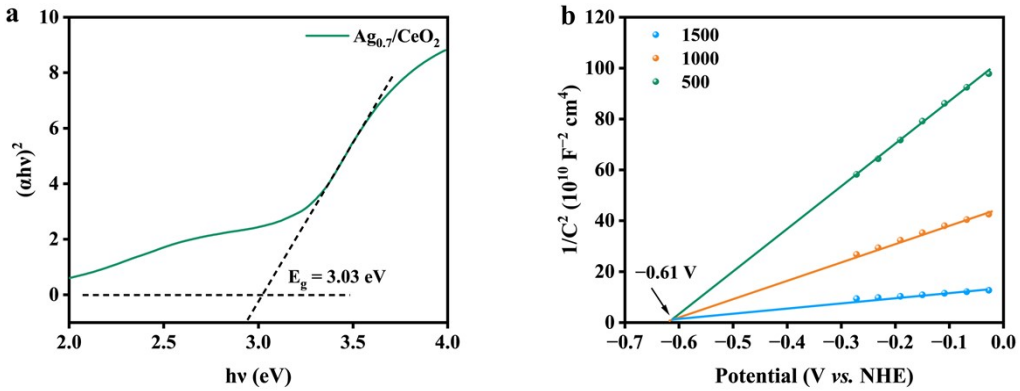

Fig. S3. (a) Tauc plot for optical-band-gap determination of $Ag_{0.7}/CeO_2$. (b) Mott-Schottky plot for $Ag_{0.7}/CeO_2$ in a 0.2 M Na_2SO_4 aqueous solution (pH = 7).

Note: To calculate the band gap energy, the following formula is used[S1]:

$$(\alpha hv)^2 = K \cdot (hv - E_g)$$

where α is the absorption coefficient, hv is the photon energy, K is a constant, and E_g is the band gap energy. As shown in **Fig. S3a**, the band gap of $Ag_{0.7}/CeO_2$ is evaluated to be 3.03 eV. In addition, the flat band position which refers to the conduction band (CB) of $Ag_{0.7}/CeO_2$ is estimated at −0.61 V *vs.* normal hydrogen electrode (NHE) according to the Mott-Schottky analysis (**Fig. S3b**). The valence band (VB) of $Ag_{0.7}/CeO_2$ is then calculated with the value of 2.42 V *vs.* NHE.

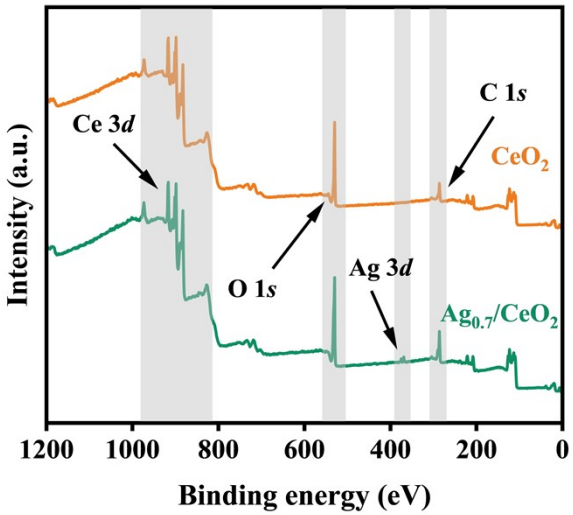

Fig. S4. High-resolution XPS spectra of CeO_2 and $Ag_{0.7}/CeO_2$.

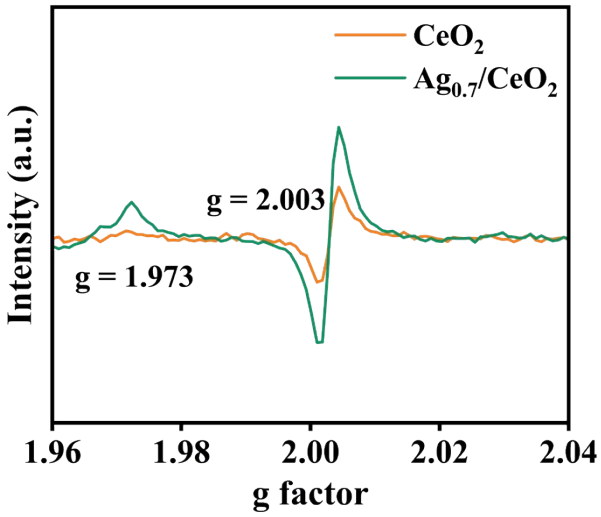

Fig. S5. EPR spectra of CeO_2 and $Ag_{0.7}/CeO_2$.

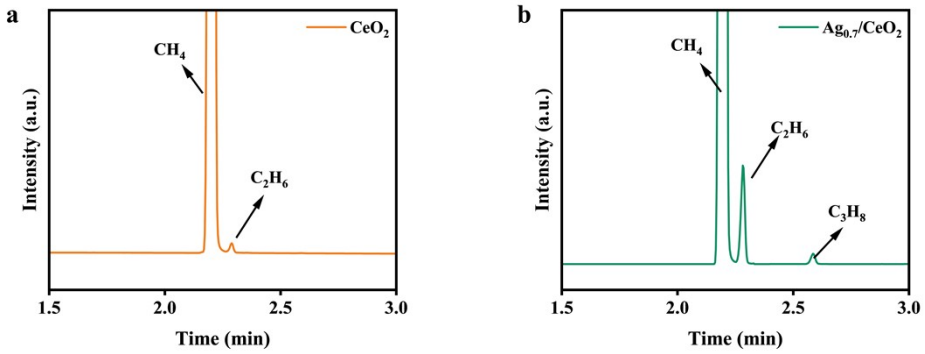

Fig. S6. GC data for photocatalytic CH_4 conversion over (a) CeO_2 and (b) $Ag_{0.7}/CeO_2$.

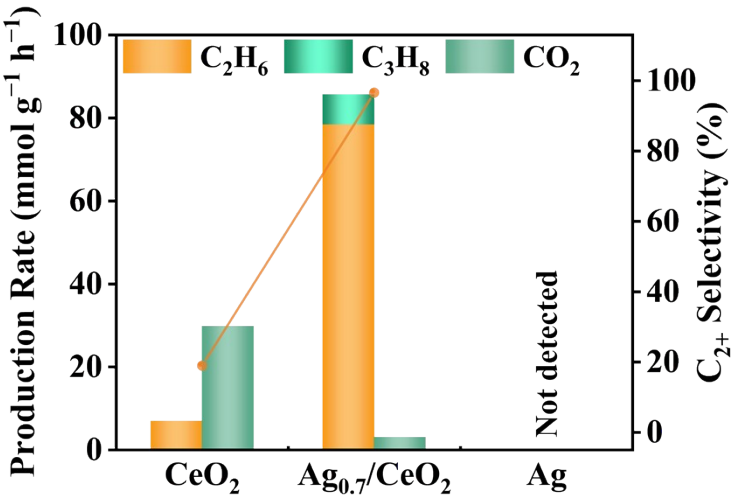

Fig. S7. The production rate of carbonaceous products in photocatalytic NOCM after 2 h light irradiation.

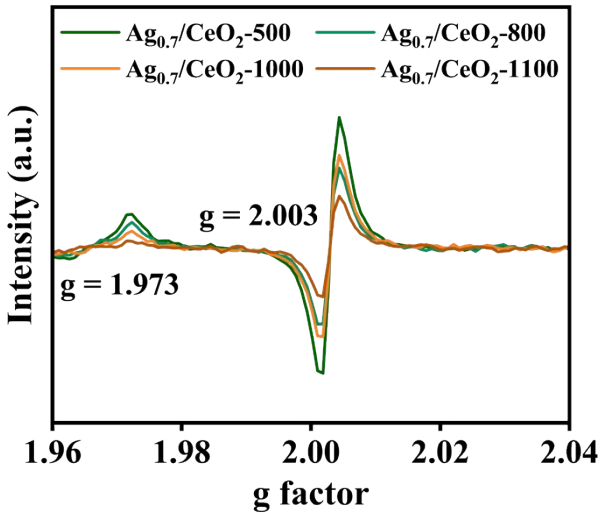

Fig. S8. EPR spectra of $Ag_{0.7}/CeO_2$-T (T = 500, 800, 1000, 1100).

Note: The absorption peak at g = 1.973, corresponding to Ce^{3+}, becomes increasingly intense with decreasing annealing temperature, reflecting a gradual increase in Ce^{3+} concentration.

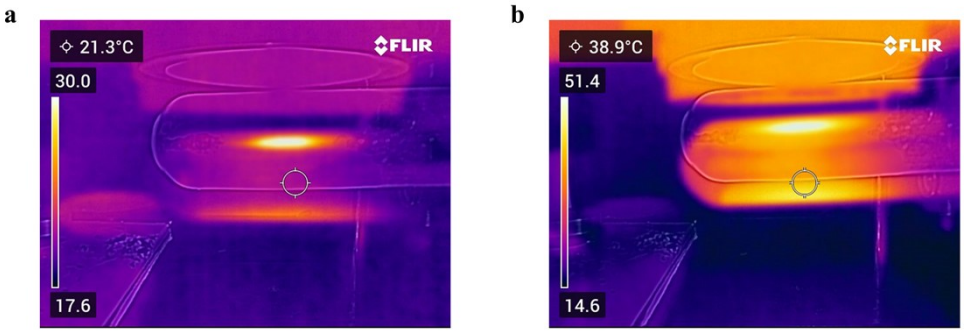

Fig. S9. Catalyst temperature variation during (a) AQY measurements and (b) regular reaction process.

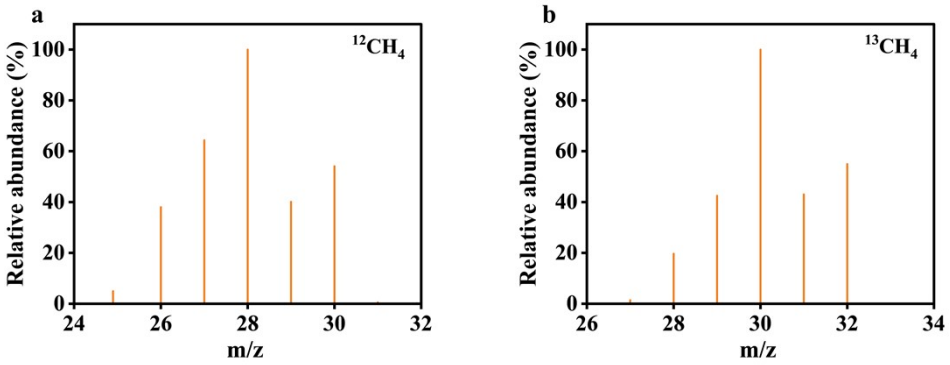

Fig. S10. (a) Mass spectra of C_2H_6 produced over $Ag_{0.7}/CeO_2$ using $^{12}CH_4$ (1 atm) as the reactant. (b) Mass spectra of C_2H_6 produced over $Ag_{0.7}/CeO_2$ using $^{13}CH_4$ (1 atm) as the reactant.

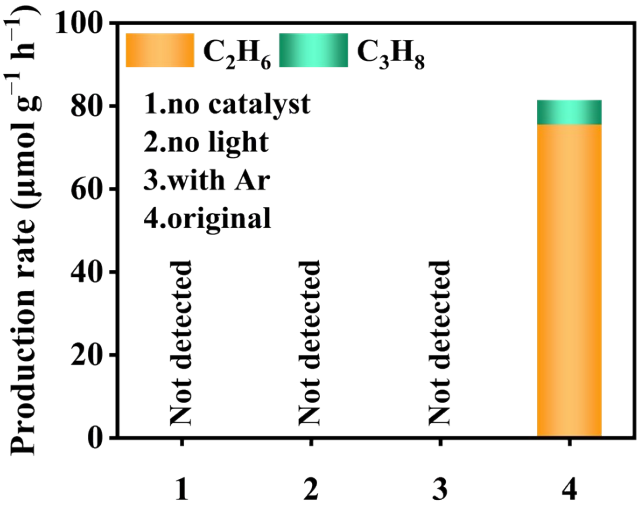

Fig. S11. Comparative experiments of $Ag_{0.7}/CeO_2$ catalyst under different conditions.

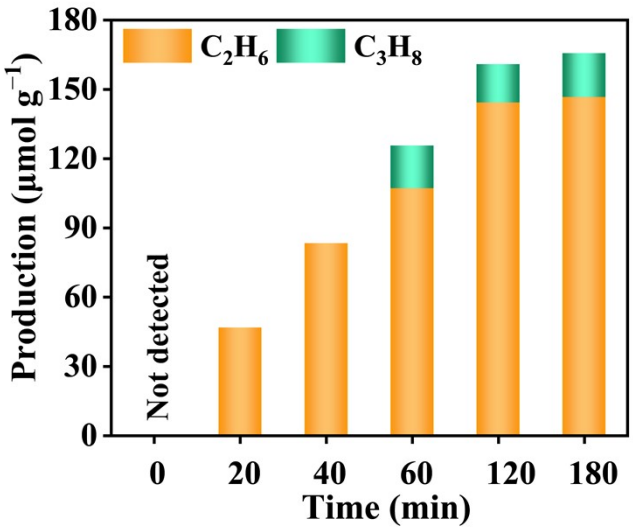

Fig. S12. Time-dependent photocatalytic C_{2+} production over $Ag_{0.7}/CeO_2$.

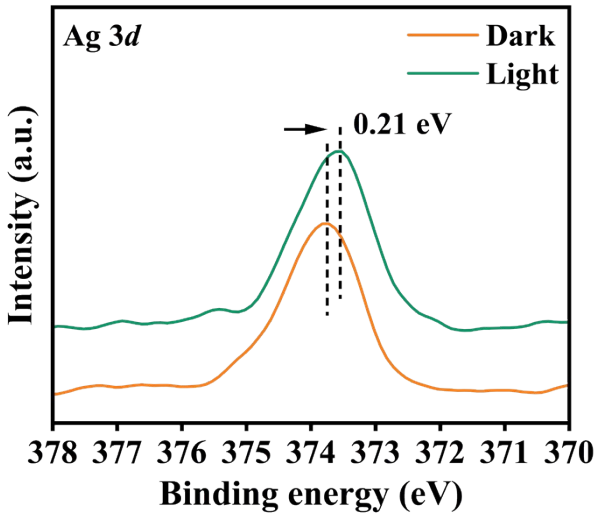

Fig. S13. In situ Ag 3*d* XPS spectra of $Ag_{0.7}/CeO_2$ under the dark condition and light irradiation.

Note: The Ag 3*d* peak exhibits a negative shift of 0.21 eV, demonstrating that Ag loses electrons under illumination. This phenomenon arises because the work function of CeO_2 (4.7 eV) is larger than that of Ag (4.2 eV), resulting in a higher Fermi level of Ag (F_m) compared to that of CeO_2 (F_s). Consequently, electrons transfer from Ag to CeO_2 until the Fermi levels equilibrate to form a new Fermi level (F_{ms}).S2 Upon light irradiation, electrons at the equilibrated Fermi level (F_{ms}) are excited to the conduction band of CeO_2, which is consistent with the observed Ce 3*d* XPS results.

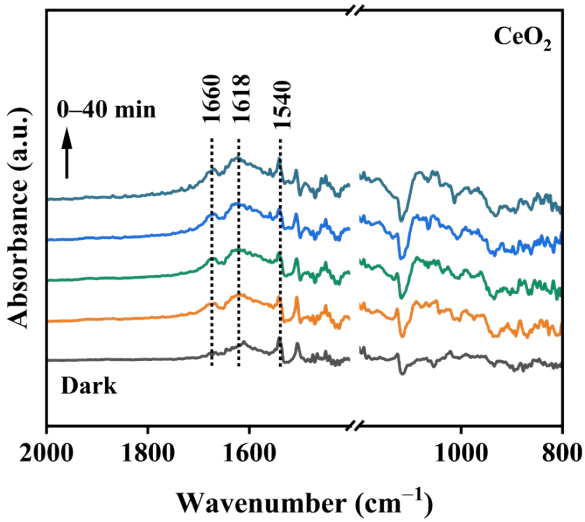

Fig. S14. In situ FT-IR spectra of photocatalytic conversion of CH_4 over CeO_2.

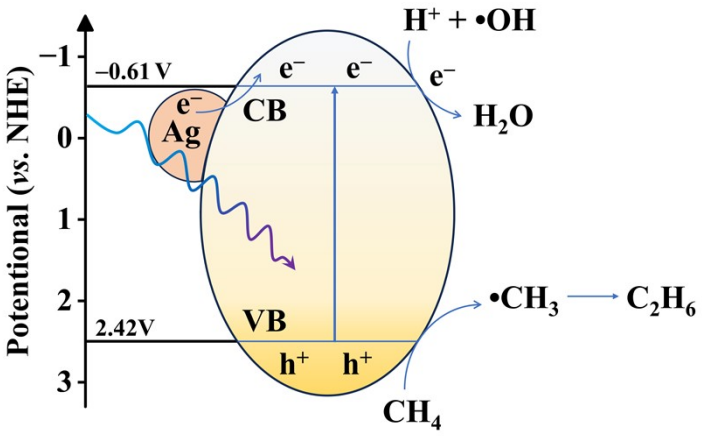

Fig. S15. Illustration of photoredox catalytic mechanism for nonoxidative coupling of CH_4 over $Ag_{0.7}/CeO_2$.

Table S1. ICP results for all composite samples.

Catalyst	Theoretical Ag loading amount (wt.%)	Experimental Ag loading amount (wt.%)
$Ag_{0.3}/CeO_2$	0.3	0.28
$Ag_{0.5}/CeO_2$	0.5	0.51
$Ag_{0.7}/CeO_2$	0.7	0.73
$Ag_{0.9}/CeO_2$	0.9	0.93
$Ag_{1.1}/CeO_2$	1.1	1.11

Table S2. The ratios of Ce^{3+} and lattice oxygen (O_{latt}) on different samples.

	Ce^{3+}	O_{latt}
CeO_2	22.11%	75.87%
$Ag_{0.7}/CeO_2$	38.93%	49.59%

Table S3. Distribution of Brønsted and Lewis acids on different samples.

Catalyst	Total acid (300 ℃)			
	Brønsted (μmol g^{-1})	Lewis (μmol g^{-1})	Total (μmol g^{-1})	B/L
CeO_2	0.61	5.02	5.63	0.12
$Ag_{0.7}/CeO_2$	1.30	13.39	14.69	0.10

Table S4. Representative works on photocatalytic nonoxidative coupling of CH_4 to C_2H_6 under identical conditions.

Entry	Catalyst	Reaction conditions	C_2H_6 production rate	Ref
1	$Ag_{0.7}/CeO_2$	300 W Xe lamp; 1 mg catalyst; 44.6 μmol CH_4	75.49 $\mu mol \cdot g^{-1} \cdot h^{-1}$	**This work**
2	Microporous Pt/TiO_2	300 W Xe lamp; 2 mg catalyst; 44.6 μmol CH_4	72 $\mu mol \cdot g^{-1} \cdot h^{-1}$	**S3**
3	Nb: TiO_2–SiO_2	300 W Xe lamp; 100 mg catalyst; 44.6 μmol CH_4	3.57 $\mu mol \cdot g^{-1} \cdot h^{-1}$	**S4**
4	MoO_3–SAPO-34	300 W Xe lamp; 200 mg catalyst; 44.6 μmol CH_4	0.45 $\mu mol \cdot g^{-1} \cdot h^{-1}$	**S5**
5	Pt/HGTS	300 W Xe lamp; 200 mg catalyst; 44.6 μmol CH_4	0.63 $\mu mol \cdot g^{-1} \cdot h^{-1}$	**S6**

Note: The activity of NOCM is highly dependent on CH_4 concentration. Therefore, to ensure comparability of the data, all activity comparisons presented in this work are based on experimental tests performed in a batch reactor using a gas mixture consisting of 1 mL of CH_4 (44.6 μmol) and argon.

Table S5. Kinetic analysis of emission decay for CeO_2 and $Ag_{0.7}/CeO_2$.

Sample	τ_1 (ns)	A_1 (%)	τ_2 (ns)	A_2 (%)	τ_a (ns)	X^2
CeO_2	11.79	0.42	1.28	99.58	1.67	1.26
$Ag_{0.7}/CeO_2$	1.15	41.87	1.15	58.13	1.14	1.24

Note: TRPL spectra decay curves were fitted by exponential decay kinetics functions and the average emission lifetime (τ_a) reflecting the overall emission decay behavior of the sample was calculated according to the following equation[S7]:

$$I(t) = A_1 \cdot e^{-\frac{t}{\tau_1}} + A_2 \cdot e^{-\frac{t}{\tau_2}}$$

$$\tau_a = \frac{A_1\tau_1^2 + A_2\tau_2^2}{A_1\tau_1 + A_2\tau_2}$$

where τ_1 and τ_2 are the emission lifetimes, while A_1 and A_2 are the corresponding amplitudes.

References

S1. N. Sha, M.-Y. Qi, Y. Zhang, H.-L. Wu, Y.-J. Xu and Z.-R. Tang, *Chem. Commun.*, 2025, **61**, 16062–16065.

S2. M. M. Khan, S. A. Ansari, J.-H. Lee, M. O. Ansari, J. Lee and M. H. Cho, *J. Colloid Interface Sci.*, 2014, **431**, 255–263.

S3. X. Feng, K. Kang, Y. Wu, J. Zhang and L. Wang, *Chem. Commun.*, 2021, **57**, 13000–13003.

S4. Z. Chen, S. Wu, J. Ma, S. Mine, T. Toyao, M. Matsuoka, L. Wang and J. Zhang, *Angew. Chem. Int. Ed.*, 2021, **60**, 11901–11909.

S5. L. Pan, S. Wu, Z. Huang, S. Zhang, L. Wang and J. Zhang, *Catal. Sci. Technol.*, 2022, **12**, 3322–3327.

S6. S. Wu, X. Tan, J. Lei, H. Chen, L. Wang and J. Zhang, *J. Am. Chem. Soc.*, 2019, **141**, 6592–6600.

S7. Y.-F. Chen, M.-Y. Qi, C.-L. Tan, Z.-R. Tang and Y.-J. Xu, *Angew. Chem. Int. Ed.*, 2025, e202513406.